Grain boundary networks in nanocrystalline alloys from atom probe tomography quantization and autocorrelation mapping

Ying Chen *,[1], Christopher A. Schuh [2]

[1] Department of Materials Science and Engineering, Rensselaer Polytechnic Institute, 110 Eighth Street, Troy, NY 12180, USA
[2] Department of Materials Science and Engineering, Massachusetts Institute of Technology, 77 Massachusetts Avenue, Cambridge, MA 02139, USA

Received ZZZ, revised ZZZ, accepted ZZZ
Published online ZZZ (Dates will be provided by the publisher.)

Keywords nanocrystalline alloys, atom probe tomography, reconstruction, local spatial autocorrelation mapping, grain boundary networks

* Corresponding author: e-mail cheny20@rpi.edu

A local spatial autocorrelation-based modelling method is developed to reconstruct nanoscale grain structures in nanocrystalline materials from atom probe tomography (APT) data, which provide atomic positions and species, with minimal noise. Using a nanocrystalline alloy with an average grain size of 16 nm as a model material, we reconstruct the three-dimensional grain boundary network by carrying out two series of APT data quantization using ellipsoidal binning, the first probing the anisotropy in the apparent local atomic density and the second quantifying the local spatial autocorrelation. This approach enables automatic and efficient quantification and visualization of grain structure in a large volume and at the finest nanoscale grain sizes, and provides a means for correlating local chemistry with grain boundaries or triple junctions in nanocrystalline materials.

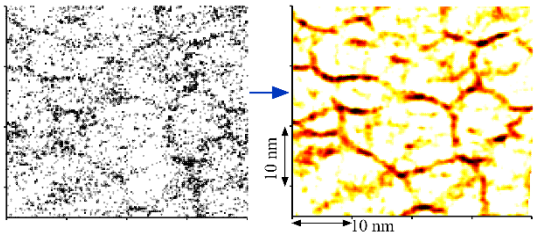

Nanoscale grain boundary networks are reconstructed from atom probe tomography data, which provide atomic positions and species for a fraction of atoms within a nanocrystalline material with an average grain size of 16 nm, using a quantization and local spatial autocorrelation-based approach.

1 Introduction Reducing the grain size in metals to the nanoscale results in a high density of grain boundaries, which strengthens the metals but renders them susceptible to coarsening [1-8]. Doping these metals produces nanocrystalline alloys that are additionally strengthened by solute atoms [9-13] and are stablized by solute segregation to grain boundaries [4, 8, 14]. In recent years, solute distribution has often been characterized by atom probe tomography (APT) [15-18], which measures element species and atomic positions with sub-nanometer resolution [19]. Segregation is usually captured by atom images, composition histograms along a line [20-29], as well as the deviation of solute frequency from the binomial distribution for random solutions [30, 31]. However, at present, there is limited quantitative understanding of how solute distribution is correlated with microstructure (e.g., all grain boundary locations), particularly at the finest nanoscale grain sizes, as APT does not directly yield interface features. Many studies have combined APT and other characterization techniques such as transmission Kikuchi diffraction [32], electron backscatter diffraction [33], and transmission electron microscopy [34]. There is also growing recognition of the need for large-scale grain reconstruction capabilities directly using APT data [35, 36]. Three-dimensional surface features (e.g., iso-surfaces) can be created from voxelization [37-39] and the marching

cubes algorithm [40]. Curvature in multilayers [41] and lattice planes [42] can also be detected and visualized. Grain boundaries (and triple junctions) were frequently identified by segregating or selected solute atoms either directly using their concentration [43] or indirectly using a distance to center of mass analysis [44]. More recently, grain boundary locations were also identified based on atomic density [45, 46] and the local curvature can be derived subsequently [45]. Significant progress has been made on crystallographic reconstructions [47-50], such as estimating grain boundary misorientation angle based on pole-fitting [51] and extracting plane orientation from real-space data [52].

In this paper, we present a local spatial autocorrelation-based method for reconstructing three-dimensional nanocrystalline grain structure from APT measurements that sample many grains in a single APT sample. Building upon prior establishments of the cube- or sphere-based voxelization method, the present approach introduces the rotating ellipsoidal voxelization or binning that accentuates grain boundaries and then further introduces a local spatial autocorrelation mapping method that drastically reduces noise and improves the connectivity of reconstructed grain boundary networks. This method is applied to an electrodeposited nanocrystalline alloy with an average grain size around 16 nm. The three-dimensional grain boundary network in this alloy was reconstructed based on APT data quantization, anisotropy in the apparent local atomic density, and local spatial autocorrelation mapping. This approach enables reconstruction of a large volume of nanocrystalline grain structure, and will lead to an automatic and efficient method for directly comparing and correlating solute composition landscape with nanoscale grain structure in a large volume.

2 Quantization The preparation and microstructure of the nanocrystalline Ni-20at% W sample have been discussed in Ref. [53]. The APT experiment was conducted at Oak Ridge National Laboratory using an Imago Scientific Instruments (currently part of CAMECA) local electrode atom probe. The measured volume is a slightly tapered cylinder with a height of 250 nm and a diameter of 64 nm at one end and 40 nm at the other. Only Ni and W atoms are counted in the analysis, and trace elements are not considered. After removing a surface layer to minimize edge effects, the remaining volume contains about 28.5 million detected atoms. The analysis in this study is performed using custom MATLAB code.

Grain boundaries have higher evaporation efficiencies than grain interiors during APT experiments [46], and can therefore be identified as regions of higher apparent local density. The local atomic density ρ is first extracted by simply using spherical bins, with their geometric center points uniformly distributed on a cubic grid with 0.25 nm spacing. The resulting local density maps for a small area at a series of bin radius r values are shown in Fig. 1a-e. Each bin is plotted as a dot, whose color darkens with increasing

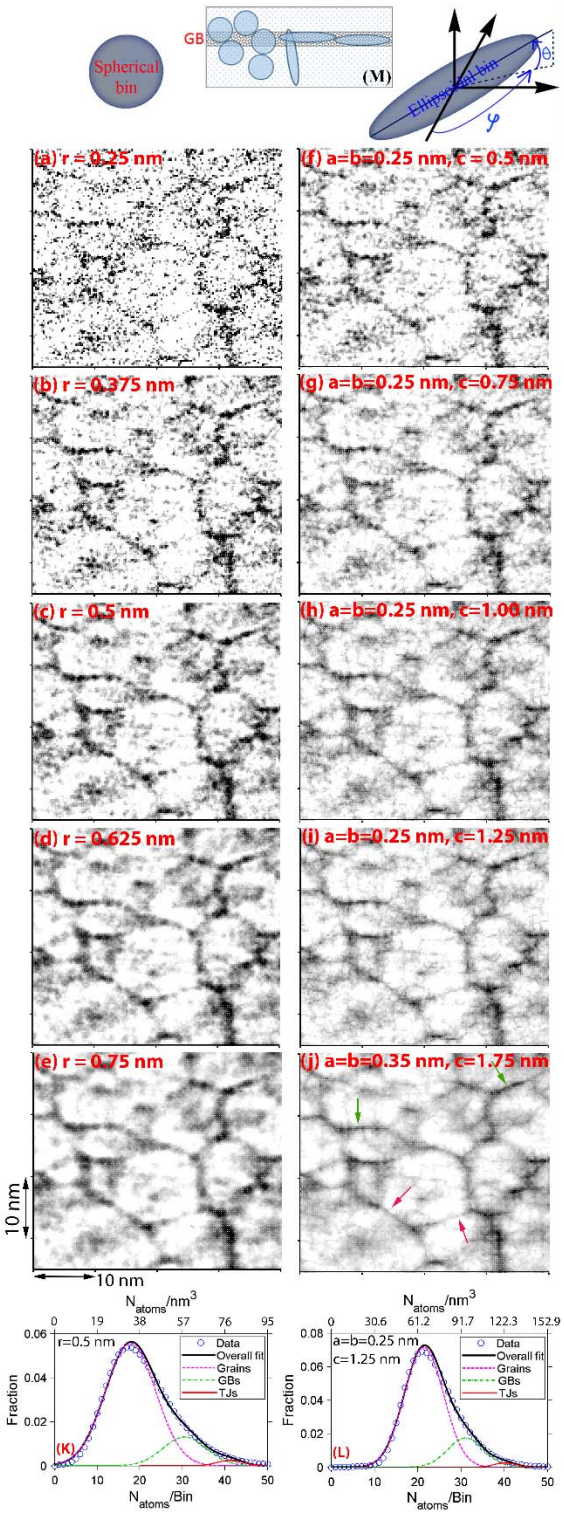

Figure 1 Vertical (x-z) sections of local density maps obtained from using spherical binning with radius r (a-e) and ellipsoidal bin with minor axes a = b and major axis c measured along the most populated bin direction at each bin center location (f-j). (k) and (l) show the histograms of local density for these two types of binning, fitted to a three-term Gaussian function.

local density. At a small bin radius such as at r = 0.25 - 0.375 nm as shown in Fig. 1a-b, a grain structure can be discerned by tracing high density bins; however, the density maps are highly granular and noisy, making it difficult to accurately identify grain boundary regions. On the other hand, using larger bins with r = 0.5 – 0.75 nm in Fig. 1c-e leads to clearer grain structures but extremely thick grain boundaries (the average width of grain boundaries seen in Fig. 1e exceeds 1.5 nm). Fig. 1k shows the histogram of local atomic density determined by this procedure with r = 0.5 nm, which deviates from the normal distribution and exhibits a high density tail related to grain boundary regions, and also includes results from fitting of Equation 1.

$$f(\rho) = \sum_{i=1}^{3} a_i exp\left[-\frac{(\rho-b_i)^2}{{c_i}^2}\right] \quad (1)$$

The three Gaussian terms in this expression correspond to three regions: grains, grain boundaries, and triple junctions, and their fitted volume fractions are f_g = 81.6%, f_{gb} = 16.5%, and f_{tj} = 1.9%, consistent with geometric expectations [54] of about 18% and 1% for the volume fractions of grain boundaries and triple junctions, respectively, at a grain size of 16 nm. This further attests to the feasibility of identifying grain boundary regions from the contrast in apparent density.

To accentuate grain boundary regions, we explore anisotropic binning of the local atomic density, with needle-like prolate ellipsoid bins (whose semi-major axis c is much larger than semi-minor axes a or b). The number of atoms whose APT coordinates lie within the ellipsoidal bin depends on the bin orientation for non-uniform atom distributions. For each bin center location, we rotate the bin in three dimensions (by changing the rotation angles φ from 0˚ to 180˚ and θ from -90˚ to 90˚ at a step size of 1.5˚; see Fig. 1) and search for the maximum density for use as the local density at the present location (defined by the bin center point). For grain boundary or triple junction locations, the most populated bin direction should lie in the grain boundary plane (Fig. 1m) or along the triple junction line, so sweeping the needle-shaped bins thus increases the chances of detecting those features at any given sampling point. Local density maps resulting from ellipsoidal binning with different bin sizes are plotted in Fig. 1f-j for the same area analyzed earlier. These maps show much less dependence on bin size as compared to those made with spherical bins, and all provide a high-quality reconstruction of the grain structures. The noise level drops and grain boundary continuity or connectivity improves slightly as the ellipsoid bin size increases from $a = b$ = 0.25 nm and c = 0.5 nm in Fig. 1f to $a = b$ = 0.35 nm and c = 1.75 nm in Fig. 1j; In Fig. 1j, the grain boundaries indicated by the red arrows are more continuous and those denoted by the green arrows are thinner than in all the other Fig.s in Fig. 1. We use the ellipsoidal bin with $a = b$ = 0.25 nm and c = 1.25 nm, and a volume of ~0.327 nm^3, corresponding to Fig. 1i, in our subsequent density analysis, as this bin size balances grain structure reconstruction quality, resolution, and computational cost. The corresponding local density

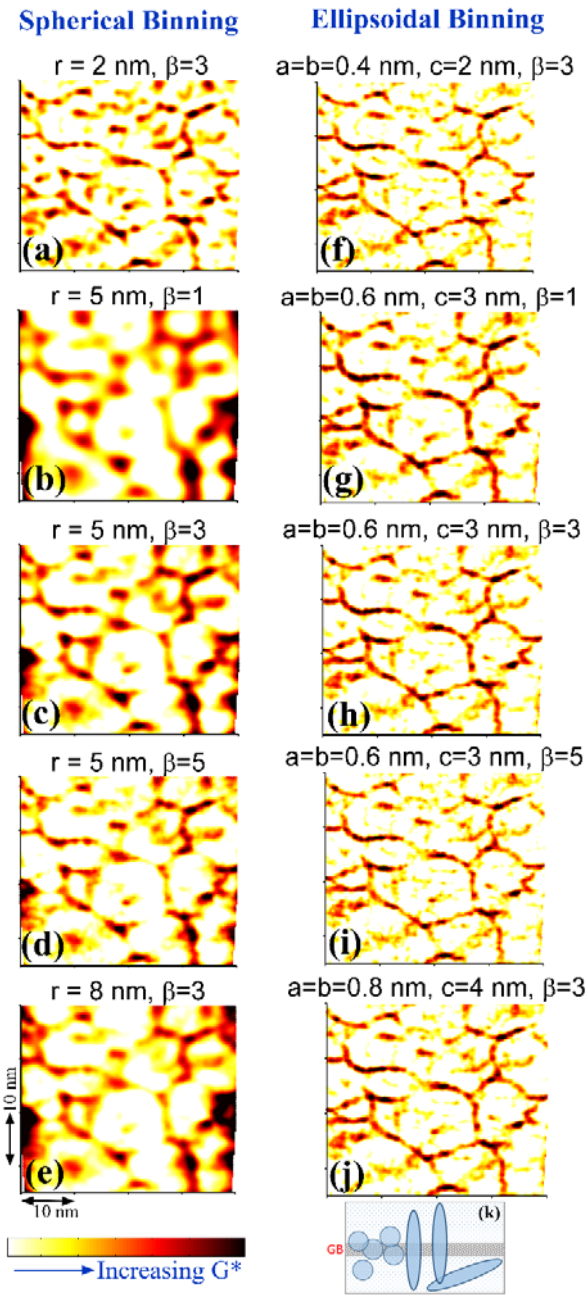

Figure 2 Maps (vertical sections) of local spatial autocorrelation G* (Equation 2) for local density obtained from spherical binning with cutoff distance r (a-e) and ellipsoidal binning with minor axes a = b and major axis c. β determines the exponential decay of the weight function with distance.

histogram, shown in Fig. 1L, also has a high density tail related to grain boundaries and triple junctions. Fitting to Equation 1 leads to f_g = 80.4%, f_{gb} = 17.9%, and f_{tj} = 1.7%, which are again in line with geometrical expectations.

Fig. 3a-c map the local density in three vertical slices of the sample with bin centers located at y = -4, 0, and 4 nm, respectively. Grain boundaries are discernible as the network connecting the highest density locations. Each of

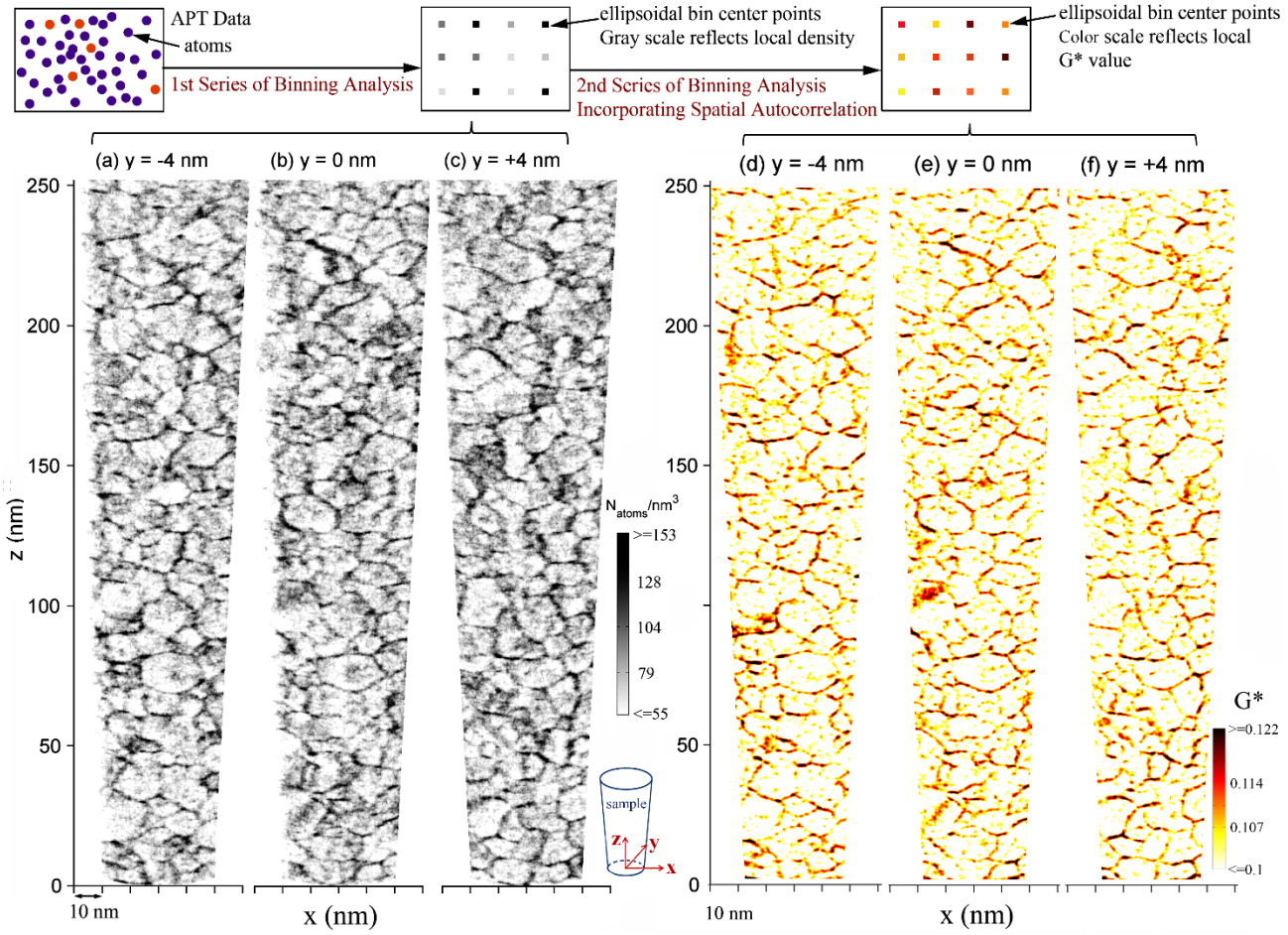

Figure 3 (a-c) Vertical sections of local density maps resulted from the 1st series of ellipsoid binning analysis. (d-f) Getis-Ord local spatial autocorrelation G* maps obtained from the 2nd series of ellipsoid binning analysis. Data for these vertical sections correspond to those at bin center points with y = -4, 0, +4 nm, respectively. Grain boundary networks can be discerned in all these maps. However, the G* maps in Fig. 3d-f show even less noise and higher contrast between grain boundaries and grain interiors, enabling high-fidelity reconstruction of nanoscale grain structures from APT data.

these maps clearly depicts a nanoscale polycrystalline grain structure. However, although ellipsoidal binning leads to rather thin grain boundary regions at a drastically reduced noise level (compared to spherical bins), a small fraction of grain interior locations also have high local densities as evident in Fig. 3a-c. Minimizing such noise will increase the accuracy of local density-based grain boundary identification, particularly when the volume fraction of grain boundaries is relatively low.

3 Local spatial autocorrelation mapping We perform a second binning analysis, but now focus on capturing the spatial autocorrelation in the local density within each new bin, so as to exclude errant noise and enhance grain boundary network-connected high density regions. The bin center points still form a cubic grid with 0.25 nm spacing. At each bin center location, the Getis-Ord local spatial autocorrelation statistic [55, 56],

$$G_i^* = \frac{\Sigma_j w_{ij}\rho_j}{\Sigma_j \rho_j} \quad (2)$$

is evaluated. In a ρ gradient field, G^* is high where high ρ values cluster (e.g., at grain boundaries), and low where low ρ values cluster (e.g., inside grains); using G^* therefore can significantly reduce spatial noise. In Equation 2, the subscripts 'i' and 'j' denote the i_{th} and j_{th} binning point, respectively; Σ_j sums over all binning points inside the current bin including the i_{th} binning point itself; ρ_j is the local atomic density at the j_{th} binning point determined in the prior ellipsoidal binning analysis. w_{ij} is a custom weight function that decays with d_{ij}, the distance between i_{th} and j_{th} binning points, and we use $w_{ij} = exp(-\beta \cdot d_{ij})$. This weight function emphasizes close neighbors, but does not smear the contrast in local density as the exponential

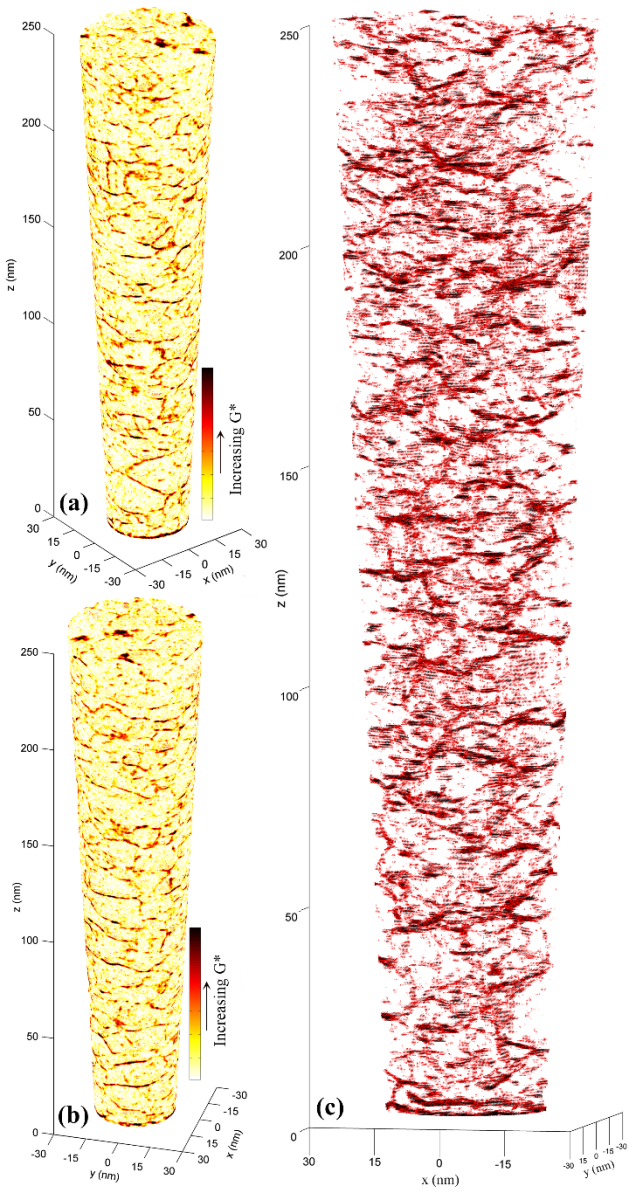

Figure 4 Three-dimensional views of the sample with the color scale reflecting G* values. (a) and (b) are the sample viewed from two different angles, and grain boundaries on or near surface are clearly visible. (c) only includes binning points with high G* values, revealing interior interface bins. The color scale in (c) conforms to the same color bar shown in (a-b).

function decays rapidly with increasing d_{ij}. Now bins much larger than those used for local density analysis are needed in order to contain sufficient grid points for the autocorrelation analysis and also contain local density variation within the bin.

As shown in Fig. 2a-e, use of spherical bins for the autocorrelation analysis generally leads to very thick and highly discontinuous grain boundaries, although triple junctions are clearly identified in most cases, regardless of the bin size r and the β value used. At $\beta = 3$, comparing Fig. 2a,c,e for $r = 2$, 5, and 8 nm, we observe that with increasing r, grain interior noise is reduced, grain boundary thickness increases while the contrast in G^* between grain boundaries and grain interior decreases. At $r = 5$ nm, comparing Fig. 2b-d for $\beta = 1$, 3, and 5 nm^{-1}, higher β results in higher contrast in G^* and thinner grain boundaries. Much more continuous grain boundary networks and thinner grain boundaries are achieved by switching to prolate ellipsoidal bins for the autocorrelation analysis. At each binning point, the bin is rotated in three dimensions by varying the rotation angles φ and θ at a step size of 3˚. For the i_{th} binning point, G_i^* is evaluated for each bin orientation, and we use the highest G_i^* value among those obtained for all bin orientations as the local G_i^*. For a grain boundary location, the highest G_i^* is usually achieved when the bin is oriented normal to the grain boundary, in which case there is well-defined gradient in ρ with distance from bin center along semi-major axis, as illustrated in Fig. 2k. As shown in Fig. 2f-j, the reconstructed grain structures are relatively insensitive to the ellipsoidal bin size and the choice of β (although the general effects of bin size and β still apply), as they all show much thinner and more continuous grain boundary networks compared to those obtained from spherical binning shown in Fig. 2a-e.

Fig. 3d-f shows the G^* map obtained using $\beta = 3$ and ellipsoidal bins with $a = b = 0.6$ nm and $c = 3$ nm for the same three slices of binning points as those in Fig. 3a-c. The highest G^* values (corresponding to red and dark red colors) are almost always found at grain boundaries, and most triple junctions show the darkest color. The autocorrelation analysis has significantly reduced the noise seen in Fig. 3a-c, and enhanced the contrast between grain boundaries and grain interiors, while capturing all key microstructural features. This reconstruction based on G^* has led to a rather continuous network of thin grain boundaries. Several characteristic three-dimensional views of the sample are provided in Fig. 4. Fig. 4a-b include more binning points, blocking the view of those in the back and only revealing those at or near the front surface; the grain boundary network seen in Fig. 4a-b therefore is mostly the intersection between grain boundary planes and the sample surface. Fig. 4c shows only binning points with the highest G^* and allows visualization through the sample, meaning most of the grain boundary planes are not shown. We therefore believe the many dark red segments in Fig. 4c correspond to triple junction lines, and the linear network in three dimensions more or less represents the triple junction line network, which plays an important role in kinetic [57, 58] and mechanical properties [59, 60] of nanocrystalline materials.

4 Conclusion It is a significant challenge for the study of nanocrystalline materials that atom probe tomography (APT) does not easily reveal the grain or grain boundary network structure. The above quantization-autocorrelation-based modeling method may serve to remedy this challenge, as we have shown the capacity to reconstruct the full three-

dimensional nanocrystalline grain structures including especially the nanoscale network of grain boundaries and triple junctions. By identifying locations of high apparent local atomic density, highlighting grain boundaries with ellipsoidal binning of those densities, and forcing connectivity of grain boundary bins via local spatial autocorrelation analysis, a clean and focused representation of the boundary network is revealed. With parallel computing, the ellipsoidal binning analysis can be carried out rather rapidly and efficiently as each grid point/location can be analyzed independently. With rapid development of APT capabilities and increasing use of APT in elucidating atomic-scale chemistry, our method will augment finest-grain-scale microstructure reconstruction capabilities and advance the understanding of structure-chemistry-property relationships in nanocrystalline alloys.

Acknowledgements Y. Chen acknowledges the RPI start-up support, and C.A. Schuh acknowledges the support from the US Army Research Office through the Institute for Soldier Nanotechnologies at MIT and under grant number W911NF-14-1-0539. We are grateful to A. Detor (formerly with MIT and currently with GE GRC) who shared APT data with us and to Oak Ridge National Laboratory (Dr. M.K. Miller) for providing user facility access and assistance.

References

[1] S. A. Sabeti, M. Pahlevaninezhad and M. Panjepour, Comp. Mater. Sci. **50**, 2104 (2011).
[2] B. S. Murty, M. K. Datta and S. K. Pabi, Sadhana **28**, 23 (2003).
[3] Y. B. Wang, J. C. Ho, X. Z. Liao, H. Q. Li, S. P. Ringer and Y. T. Zhu, Appl. Phys. Lett. **94**, 011908 (2009).
[4] A. A. Talin, E. A. Marquis, S. H. Goods, J. J. Kelly and M. K. Miller, Acta Mater. **54**, 1935 (2006).
[5] A. F. Jankowski, C. K. Saw and J. P. Hayes, Thin Solid Films **515**, 1152 (2006).
[6] G. D. Hibbard, K. T. Aust and U. Erb, Acta Mater. **54**, 2501 (2006).
[7] W. Voegeli, K. Albe and H. Hahn, Nucl. Instrum. Meth. B **202**, 230 (2003).
[8] R. A. Andrievski, J. Mater. Sci. **38**, 1367 (2003).
[9] C. C. Koch, K. M. Youssef, R. O. Scattergood and K. L. Murty, Adv. Eng. Mater. **7**, 787 (2005).
[10] C. Suryanarayana and C. C. Koch, Hyperfine Interact. **130**, 5 (2000).
[11] M. A. Meyers, A. Mishra and D. J. Benson, Prog. Mater. Sci. **51**, 427 (2006).
[12] M. Dao, L. Lu, R. J. Asaro, J. T. M. De Hosson and E. Ma, Acta Mater. **55**, 4041 (2007).
[13] K. S. Kumar, H. Van Swygenhoven and S. Suresh, Acta Mater. **51**, 5743 (2003).
[14] A. J. Detor and C. A. Schuh, J. Mater. Res. **22**, 3233 (2007).
[15] D. N. Seidman, Annu. Rev. Mater. Res. **37**, 127 (2007).
[16] T. F. Kelly and D. J. Larson, MRS Bulletin **37**, 150 (2012).
[17] T. F. Kelly and M. K. Miller, Rev. Sci. Instrum. **78**, 031101 (2007).
[18] D. N. Seidman and K. Stiller, MRS Bulletin **34**, 717 (2009).
[19] F. Vurpillot, B. Gault, B. P. Geiser and D. J. Larson, Ultramicroscopy **132**, 19 (2013).
[20] M. K. Miller, J Mater Sci **41**, 7808 (2006).
[21] B. Färber, E. Cadel, A. Menand, G. Schmitz and R. Kirchheim, Acta Mater. **48**, 789 (2000).
[22] E. A. Marquis, M. K. Miller, D. Blavette, S. P. Ringer, C. K. Sudbrack and G. D. W. Smith, MRS Bulletin **34**, 725 (2009).
[23] P. Choi, M. da Silva, U. Klement, T. Al-Kassab and R. Kirchheim, Acta Mater. **53**, 4473 (2005).
[24] K. Seto, D. J. Larson, P. J. Warren and G. D. W. Smith, Scripta Mater. **40**, 1029 (1999).
[25] Y. Amouyal, Z. Mao and D. N. Seidman, Appl. Phys. Lett. **93**, 201905 (2008).
[26] D. J. Larson, A. Cerezo, J. Juraszek, K. Hono and G. Schmitz, MRS Bulletin **34**, 732 (2009).
[27] L. J. Lauhon, P. Adusumilli, P. Ronsheim, P. L. Flaitz and D. Lawrence, MRS Bulletin **34**, 738 (2009).
[28] P. Stender, Z. Balogh and G. Schmitz, Phys. Rev. B **83**, 121407 (2011).
[29] K.-M. Yin, A. H. King, T. E. Hsieh, F.-R. Chen, J. J. Kai and L. Chang, Microsc. Microanal. **3**, 417 (1997).
[30] M. P. Moody, L. T. Stephenson, A. V. Ceguerra and S. P. Ringer, Microsc. Res. Techniq. **71**, 542 (2008).
[31] P. Felfer, A. V. Ceguerra, S. P. Ringer and J. M. Cairney, Ultramicroscopy **150**, 30 (2015).
[32] K. Babinsky, W. Knabl, A. Lorich, R. De Kloe, H. Clemens and S. Primig, Ultramicroscopy (2015).
[33] S. Meher, P. Nandwana, T. Rojhirunsakool, J. Tiley and R. Banerjee, Ultramicroscopy **148**, 67 (2015).
[34] M. Herbig, P. Choi and D. Raabe, Ultramicroscopy **153**, 32 (2015).
[35] J. M. Cairney, K. Rajan, D. Haley, B. Gault, P. A. J. Bagot, P.-P. Choi, P. J. Felfer, S. P. Ringer, R. K. W. Marceau and M. P. Moody, Ultramicroscopy (2015).
[36] S. K. Suram and K. Rajan, Ultramicroscopy **132**, 136 (2013).
[37] S. Srinivasan, K. Kaluskar, S. Dumpala, S. Broderick and K. Rajan, Ultramicroscopy (2015).
[38] O. C. Hellman, J. B. du Rivage and D. N. Seidman, Ultramicroscopy **95**, 199 (2003).
[39] K. L. Torres, M. Daniil, M. A. Willard and G. B. Thompson, Ultramicroscopy **111**, 464 (2011).
[40] W. E. Lorensen and H. E. Cline, presented at the ACM siggraph computer graphics, 1987 (unpublished).
[41] D. J. Larson, A. K. Petford-Long, A. Cerezo and G. D. W. Smith, Acta Mater. **47**, 4019 (1999).
[42] H. Gnaser, Surface and Interface Analysis **46**, 383 (2014).
[43] Z. Balogh, P. Stender, M. Chellali and G. Schmitz, Metall and Mat Trans A **44**, 4487 (2013).
[44] P. Felfer, A. Ceguerra, S. Ringer and J. Cairney,

Ultramicroscopy **132**, 100 (2013).
[45] P. V. Liddicoat, X.-Z. Liao, Y. Zhao, Y. Zhu, M. Y. Murashkin, E. J. Lavernia, R. Z. Valiev and S. P. Ringer, Nat Commun **1**, 63 (2010).
[46] S. K. Samudrala, P. J. Felfer, V. J. Araullo-Peters, Y. Cao, X. Z. Liao and J. M. Cairney, Ultramicroscopy **132**, 158 (2013).
[47] V. J. Araullo-Peters, B. Gault, S. L. Shrestha, L. Yao, M. P. Moody, S. P. Ringer and J. M. Cairney, Scripta Mater. **66**, 907 (2012).
[48] L. Yao, M. P. Moody, J. M. Cairney, D. Haley, A. V. Ceguerra, C. Zhu and S. P. Ringer, Ultramicroscopy **111**, 458 (2011).
[49] L. Yao, S. P. Ringer, J. M. Cairney and M. K. Miller, Scripta Mater. **69**, 622 (2013).
[50] B. Gault, M. P. Moody, J. M. Cairney and S. P. Ringer, Materials Today **15**, 378 (2012).
[51] J. Takahashi, K. Kawakami and Y. Kobayashi, Ultramicroscopy **140**, 20 (2014).
[52] V. J. Araullo-Peters, A. Breen, A. V. Ceguerra, B. Gault, S. P. Ringer and J. M. Cairney, Ultramicroscopy **154**, 7 (2015).
[53] A. J. Detor, M. K. Miller and C. A. Schuh, Phil. Mag. Lett. **87**, 581 (2007).
[54] Y. Chen and C. A. Schuh, J. Appl. Phys. **101**, 063524 (2007).
[55] A. Getis and J. K. Ord, Geogr. Anal. **24**, 189 (1992).
[56] J. K. Ord and A. Getis, Geogr. Anal. **27**, 286 (1995).
[57] Y. Chen and C. A. Schuh, Scripta Mater. **57**, 253 (2007).
[58] M. Wegner, J. Leuthold, M. Peterlechner, X. Song, S. Divinski and G. Wilde, J. Appl. Phys. **116**, 093514 (2014).
[59] Y. Zhou, U. Erb, K. T. Aust and G. Palumbo, Scripta Mater. **48**, 825 (2003).
[60] I. A. Ovid'ko and A. G. Sheinerman, Acta Mater. **52**, 1201 (2004).